PAPER

Check for updates

Ionic liquid microemulsion-mediated heterogels with bicontinuous conductive channels for an ionic flexible sensor

Yufan Wang,† Yue Wang,† Li Qin, Zhuo Zhang and Yang Yu [ID] *

The incorporation of microstructural designs into flexible sensors has emerged as a potent strategy to enhance the capability of capturing fine information. Herein, an ionic liquid microemulsion-template strategy is presented to fabricate conductive heterogels with a bicontinuous structure of interpenetrating hydrophilic and hydrophobic phases, in which the hydrophilic ionic liquid domain functions as ion-rich channels and provides conductivity. The hydrophobic polymer domain serves as a supporting skeleton. Amphiphilic zwitterions anchored at the phase interface serve as effective ion transport sites to improve ion conduction. The bicontinuous structure enhances the mechanical performance, anti-swelling, thermal stability and ion conductivity of the heterogels. The assembled flexible sensor exhibits the sensitive detection of subtle muscle movements and specific recognition of speech, weight and temperature. This study is expected to provide innovative insights into the design and regulation of ion channels in flexible sensing devices.

1. Introduction

As the core of human–machine interconnection information technology, flexible sensing technology has opportunities for continuous reformation and innovation.[1] Compared with electronic sensing, ionic sensing offers superior sensitivity, signal stability, and electromagnetic interference immunity;[2,3] thus, ionic flexible sensors are promising material candidates to be employed in various applications such as personalized healthcare,[4] brain–computer interfaces,[5] and soft robotics.[6] At present, ionic flexible sensors primarily encompass hydrogels,[7] organogels,[8] ionic conductive elastomers,[9] and ionogels.[10] The performance of hydrogels and organogels is often compromised by the issue of solvent volatilization.[11] However, most solvent-free ion-conductive elastomers are often limited by poor ionic conductivity.[12] Based on the fascinating properties of ionic liquids, such as non-volatility, non-flammability, excellent electrothermal stability and conductivity,[13] ionogels exhibit significant potential in cutting-edge fields such as solid-state electrolytes,[14] flexible sensing and human–computer interaction.[15] Thus, ionogels are highly advantageous and promising core materials for constructing ionic flexible sensors.

Ionic flexible sensors provide strain feedback based on ion diffusion changes in the ion-sensitive layer.[16] The deformed ion-sensitive layer causes a change in the path and rate of ion

diffusion.[17] Beyond the materials of the ion-sensitive layer, a well-designed microstructure critically determines sensor performance by regulating ion transport paths and migration efficiency.[18,19] To further improve the performance of ionic flexible sensors, a common strategy is to design and optimize the internal microstructure of the ion-sensitive layer.[20] The advancement from simple flexible supports to the design of microstructural functional matrices is of great significance for high-performance flexible sensors.[21] The bicontinuous structure consists of interpenetrating and continuous channels, providing a three-dimensional percolating network for ion transport.[22] This architecture avoids the tortuous paths and obstructions that are common in traditional porous materials, enabling ions to diffuse rapidly and transport uniformly and thereby significantly enhancing ionic conductivity.[23] Ge *et al.* reported a UV-curable ionogel with bicontinuous nanostructures.[24] Utilizing the polarity contrast between benzyl acrylate (BA) and poly(ethylene glycol) methyl ether methacrylate (PEGMAPEGMA), photopolymerization at specific ratios produced a bicontinuous interpenetrating nanostructure, enabling ordered and efficient ion liquid migration along the $-CH_2-O-CH_2-$ segments of the PEGMA phase. In addition, the polymer–solvent affinity provides another crucial driving force for phase separation. For instance, Huang *et al.* constructed a DMSO–hydrophobic ionic liquid binary solvent that exploits differential polymer–water affinity to drive phase separation.[25] Hydrophilic monomer acrylic acid (AAc) and hydrophobic monomer 2-ethylhexyl acrylate (EHA) copolymerized to form a well-defined network structure within the dual-solvent system. Subsequently, the water-mediated displacement of DMSO drove

School of Chemistry and Chemical Engineering, Qilu Normal University, Jinan, 250200, China. E-mail: yuyang@qlnu.edu.cn

† These authors contributed equally to this work. They should thus be considered co-first authors.

phase separation to form a bicontinuous gel. The engineered gels were utilized as wearable sensors with long-term reliability and wide sensing ranges. However, for phase separation triggered by solvent compatibility disparities, it is often necessary to precisely select the solvent or tailor the molecular structure.[26] Furthermore, physical techniques like 3D holographic lithography and direct laser writing struggle with precise pore size control at the micro–nano scale.[27]

The heterogeneous bicontinuous microemulsion, which combines the characteristics of both hydrophilic and hydrophobic phases,[28] provides a straightforward route for constructing bicontinuous structures. Therefore, ionic liquids as the foundational component to construct bicontinuous microemulsions merge into interpenetrating channels with intrinsic properties of ILs.[29] This functional integration strategy enables efficient ion transport while concurrently enhancing material stability. Herein, we constructed heterogels with bicontinuous conductive channels using an ionic liquid microemulsion-based template. The mixed solutions of the hydrophilic ionic liquid(1-ethyl-3-ethylimidazoliumbis(triuoromethanesulfonyl)-imide, C2MImTFSI), hydrophobic monomer (1,12-dodecanediol dimethacryalate C12-DMA), and amphiphilic zwitterion (3-(1-dodecyl-3-imidazolio) propanesulfonate, ZC12) were co-assembled into bicontinuous microemulsions. Subsequently, *in situ* photopolymerization effectively preserves the microstructure. The obtained heterogel effectively mitigates the humidity sensitivity inherent in conventional ionogels *via* hydrophilic–hydrophobic modulation.[30] Moreover, the bicontinuous microstructure coupled with interfacial zwitterionic groups establishes efficient ion transport pathways. These attributes are essential for enabling ionic flexible sensors to achieve precise micro-strain monitoring and rapid detection of weight and temperature variations.

2. Experimental section

2.1 Materials

1-Dodecylimidazole (97%, Shanghai Aladdin Biochemical Technology Co., Ltd); 1,3-propanesultone (99%, Beijing J&K Scientific Ltd); acetone (99.5%, Sinopharm Chemical Reagent Co., Ltd); 1-ethyl-methylimidazoliumbis(trifluoromethanesulfonyl)-imide (C2MImTFSI; 99%, Beijing J&K Scientific Ltd); 1,12-dodecanediol dimethacrylate (C12-DMA, 95%, Shanghai Aladdin Biochemical Technology Co., Ltd); 2-hydroxy-2-methylpropiophenone (1173 photoinitiator, Sigma-Aldrich Inc.); artificial sweat (pH = 6.5, Shanghai Macklin Biochemical Co., Ltd).

2.2 Synthesis of 3-(1-dodecyl-3-imidazolio)propanesulfonate (ZC12)

ZC12 was synthesized according to the literature method.[31,32] In brief, 1-dodecylimidazole was dissolved in acetone. Then, an equimolar amount of 1,3-propanesultone in acetone was slowly added to the above solution at room temperature. The reaction mixture was then stirred for 3 days. Subsequently, the solution was filtered under reduced pressure. Finally, ZC12 was obtained by drying under vacuum at room temperature. The ^{1}H NMR

spectra of ZC12 were obtained using a Bruker Avance 400 MHz NMR at 25 °C with DMSO solvents, as shown in Fig. S1. δ (relative to TMS): 9.190 (1H, s), 7.805 (1H, t), 7.785 (1H, t), 4.303 (t, 2H), 4.148 (2H, t), 2.402 (2H, t), 2.094 (2H, quint), 1.783 (2H, m), 1.239 (18H, m), 0.855 (t, 3H).

2.3 Preparation of heterogels

The heterogels were prepared by the *in situ* photopolymerization of an ionic liquid-based emulsion. First, the emulsion was prepared by mixing C2MImTFSI and C12-DMA in the presence of a surfactant (ZC12) and photoinitiator 1173. The mixing ratios of the chemical ingredients in the heterogels are shown in Table S1. Then, the emulsion in the glass mold was irradiated using a UV arc lamp with an intensity of 9 mW cm^{-2} for 15 min at room temperature from both the top and bottom surfaces of the plates to obtain free-standing heterogels.

2.4 Characterization

^{1}H NMR spectra were recorded using a Bruker Advance 400 spectrometer at 400 MHz. DSC measurements were carried out using a PerkinElmer 8500 calorimeter at a heating rate of 10 °C min^{-1} under a flow of nitrogen. Fourier transform infrared spectroscopy (FT-IR) was recorded using a Nicolet iS5 spectrometer (Thermo Fisher). TGA measurements were carried out using Mettler TGA2 with a heating rate of 10 °C min^{-1} under a flow of nitrogen. An optical microscope (CNOPTEC L40Pro) was used to observe the structural types of the emulsions. The cross-sectional morphology of the heterogels was investigated using a scanning electron microscope (ZEISS Sigma300). The EDS mapping of the F element was carried out using an energy spectrometer (Oxford Xplore 30). The dynamic rheological behaviors of the heterogels were determined using a rheometer (Anton Paar MCR102e). Small-angle X-ray scattering (SAXS) measurements were carried out on a SAXSess mc2 X-ray scattering system (Anton Paar). Contact angle measurements were carried out using a commercial drop shape analyzer (Tracker, France Teclis) at room temperature. Ionic conductivity and sensing tests were carried out using a CHI760D electrochemical analyzer/workstation.

2.5 Rheological property measurements

The dynamic rheological behaviors of the heterogels were tested at room temperature. All heterogels were characterized through frequency scanning (0.01–100 Hz). A cone-plate sensor with a 20 mm diameter and a 1u cone angle was used. The temperature was maintained at 25 °C.

2.6 Swelling measurements

The swelling ratio of the heterogels was determined by recording the weight of the heterogels after immersion in deionized water or artificial sweat for varying durations. The calculation formula is as follows:

$$\text{Swelling ratio}(\%) = \frac{\text{swelling mass} - \text{initial mass}}{\text{initial mass}} \times 100\%.$$

2.7 Thermal stability measurements

The heterogels were subjected to thermal exposure in an oven at 80 °C (relative humidity $\approx$ 0%) to evaluate their thermal stability by monitoring mass evolution over predetermined time intervals. The calculation formula is specified as follows:

$$\text{Residual mass}(\%) = \frac{\text{mass after heating}}{\text{initial mass}} \times 100\%.$$

2.8 Ionic conductivity measurements

The ionic conductivities of the heterogels were investigated using the alternating current impedance method at a frequency of $100–10^6$ Hz with 0.3 mV oscillating voltage using a stainless steel cell consisting of a pair of stainless steel electrodes and a Teflon spacer. During the investigation of the temperature–conductivity relationship, the assembled stainless steel cell must be maintained at each target temperature for 30 minutes to achieve thermal equilibrium prior to measurement.

2.9 Sensing performance measurements

Based on a comprehensive evaluation of all the performance metrics, the $C_{12}30$-25 heterogel was used to fabricate the ionic flexible sensor. The heterogel was precisely positioned at key facial landmarks, including the glabella, oral commissures, and lateral canthi, to capture micro-scale muscular contractions. For laryngeal applications, the mounted sensor achieved word-level discrimination through real-time monitoring of laryngeal vibrations and subtle tissue deformation. In the quantitative mechanosensitivity assessment, graded standard weights were applied to the sensor surface to establish its pressure–response relationship. Additionally, palm-mounted sensors were used to assess thermal sensitivity through continuous grasping of water cups at different temperatures (4 °C, 30 °C, 50 °C and 60 °C).

3. Results and discussion

3.1 Preparation and structural characterization of heterogels

In this work, we used an ionic liquid microemulsion-based template strategy to fabricate heterogels featuring bicontinuous architectures, as shown in Fig. 1. Initially, the two immiscible liquids of the ionic liquid 1-ethyl-3-methylimidazolium bis(trifluoromethanesulfonyl)-imide (C2MImTFSI) and the monomer 1,12-dodecanediol dimethacryalate (C12-DMA) were mixed in the presence of the amphiphilic zwitterion 3-(1-dodecyl-3-imidazolio) propanesulfonate (ZC12). By tuning the compositional ratio, various emulsions can be generated, which are then subjected to *in situ* photopolymerization to yield heterogels with distinct microstructures. In bicontinuous heterogel networks, the polymer C12-DMA acts as a hard framework to lock the two-phase structure, endowing the heterogel with macroscopic solid characteristics to achieve self-support. The IL C2MImTFSI as a soft plasticizing phase imparts flexibility and elasticity to the heterogel, while the continuous IL phase constructs a high-speed pathway for ion transport. Furthermore, ILs as high-flux natural ion carriers require no additional conductive salts to achieve conductivity, thereby avoiding the salting-out issue.[33] The densely packed amphiphilic zwitterions ZC12 on the bicontinuous interface form a "soft" interfacial layer that facilitates ion migration.[34] Acting as active sites, the zwitterionic groups guide ions along the surface for long-range, rapid transport, which significantly lowers the energy barrier for ion transport near the interface,[35] thereby promoting interfacial ion diffusion.

The bicontinuous microemulsion was achieved by adjusting the composition ratio of the ternary components, as shown in Table S1. The diagram and digital images in Fig. 2a and b show the appearance and microstructure of the emulsions. At low ZC12 contents ($C_{12}30$-10 and $C_{12}30$-15), the obtained emulsions were opaque and thermodynamically unstable. Corresponding microstructural imaging also displays a droplet-type emulsion, with droplet dimensions falling in the range of 10–30 μm (Fig. 2b). At 20–30 wt% of ZC12 ($C_{12}30$-20, $C_{12}30$-25, and $C_{12}30$-30), the thermodynamically stable and transparent bicontinuous microemulsions were obtained. The uniform dark field under optical microscopy is consistent with the isotropic nature of the bicontinuous microemulsion. However, emulsions with higher zwitterion content ($C_{12}30$-35 and $C_{12}30$-40)
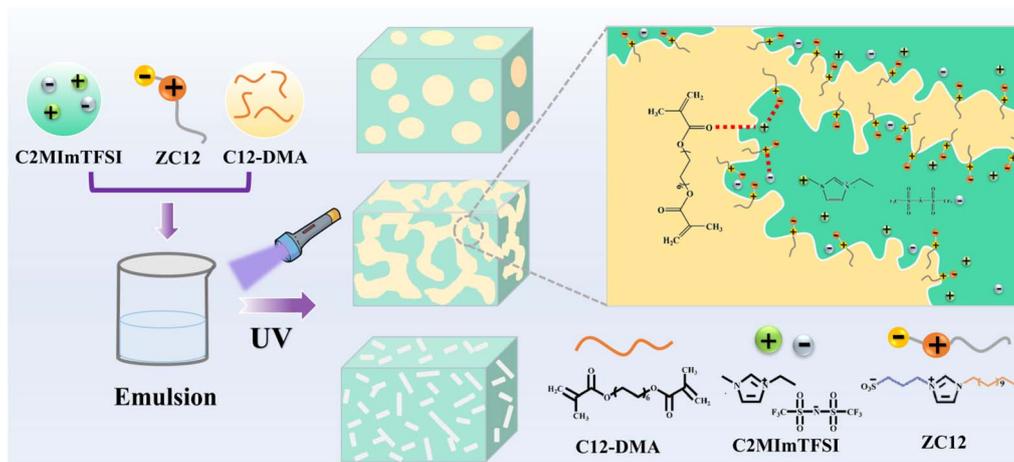

Fig. 1 Schematic of the fabrication process of the bicontinuous heterogels and bicontinuous conductive channels.
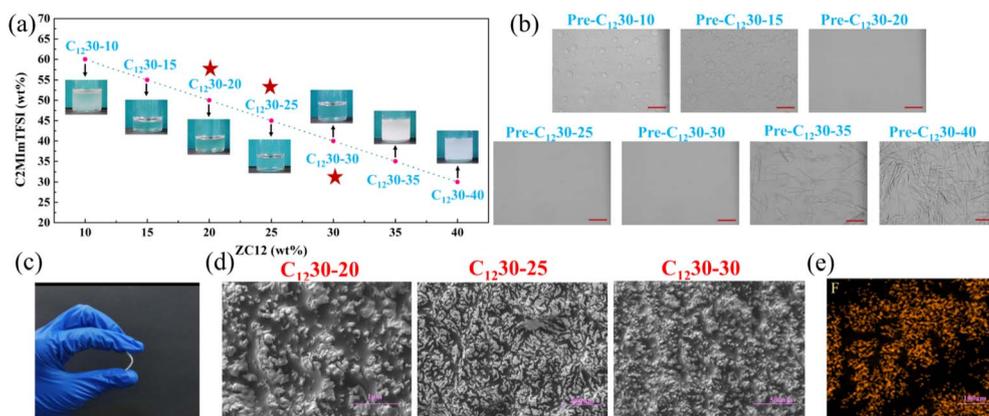
Fig. 2 (a) Diagram and images of different emulsion samples. (b) Optical micrographs of different emulsion samples. The scale bar is 100 μm. (c) Digital images of heterogels. (d) SEM images of $C_{12}30-20$, $C_{12}30-25$, and $C_{12}30-30$. (e) EDS mapping of the F element of the $C_{12}30-25$ heterogel.

exhibited precipitation, driven by the tendency of zwitterions at elevated concentrations to self-associate into a precipitating "internal salt" structure.[36] To preserve the bicontinuous structure of the microemulsion, we employed an *in situ* photopolymerization strategy. After photopolymerization, a flexible and self-supporting heterogel was obtained, as shown in Fig. 2c. To verify whether the bicontinuous structure is well preserved in the heterogels, scanning electron microscopy (SEM) was performed. Fig. 2d illustrates the cross-sectional SEM images of $C_{12}30-20$, $C_{12}30-25$ and $C_{12}30-30$. However, the phase states of $C_{12}30-20$ and $C_{12}30-30$ were transformed after photopolymerization. Only the interpenetrating bicontinuous structure of $C_{12}30-25$ remained well preserved, in which the dark regions represented the hydrophilic domains, while the bright areas represented the hydrophobic domains. Since the F elemental is exclusively present in the ionic liquid, the distinct distribution observed in the F elemental EDS images also confirms the presence of the bicontinuous structure in $C_{12}30-25$, as shown in Fig. 2e. Further structural information on emulsions and heterogels was obtained by small-angle X-ray scattering (SAXS) experiments. As shown in Fig. 3a, for

unpolymerized emulsions, the droplet emulsions (Pre-$C_{12}30-10$ and Pre-$C_{12}30-15$) exhibit a broad scattering peak, whereas the bicontinuous microemulsions (Pre-$C_{12}30-20$, Pre-$C_{12}30-25$, and Pre-$C_{12}30-30$) show distinct scattering peaks. After photopolymerization, the scattering peak persists in the $C_{12}30-25$ heterogel, confirming the retention of the bicontinuous structure, as shown in Fig. 3b. However, for $C_{12}30-20$, the scattering peak of the bicontinuous structure is significantly diminished probably due to the insufficient amount of the amphiphilic ZC12 to stabilize the interface, as C12-DMA often exhibits stronger hydrophobicity after polymerization.[37] For $C_{12}30-30$, the significant attenuation of the bicontinuous peak intensity indicates probable phase separation of the zwitterion resulting from increased intramolecular self-aggregation at high content.[38]

To elucidate the interactions between ZC12 and C2MImTFSI within bicontinuous ionic channels, the ^{1}H NMR and FT-IR analyses were performed. The ^{1}H NMR spectra were based on the equivalent ratio of the binary components within the heterogels. A high content of zwitterions typically induces molecular self-association. The introduction of ionic liquids disrupts this self-association structure of zwitterions, which leads to the formation of new ion pairs,[39] resulting in an electrostatic shielding effect on the zwitterions.[36] Consequently, Ha exhibits an upfield shift with increasing IL content, as shown in Fig. 3c. Conversely, as zwitterions promote the dissociation of ionic liquids, generating a greater population of free ions, the chemical shift of proton Hb moves downfield upon the addition of zwitterions (Fig. 3c). FT-IR spectroscopy further corroborates this ionic reorganization phenomenon, as shown in Fig. 3d. Due to the strong electron-withdrawing effect of the trifluoromethyl group (–CF₃),[40] the S=O stretching vibration peak at a high wavenumber is assigned to C2MImTFSI. With increasing ZC12 content, ion dissociation induces a blue shift in the S=O stretching vibration peak of C2MImTFSI. Conversely, the electrostatic shielding from ionic liquids results in a red shift in the sulfonate groups of ZC12. These results further demonstrate that within the bicontinuous channel structure, ionic liquids can achieve more efficient transport
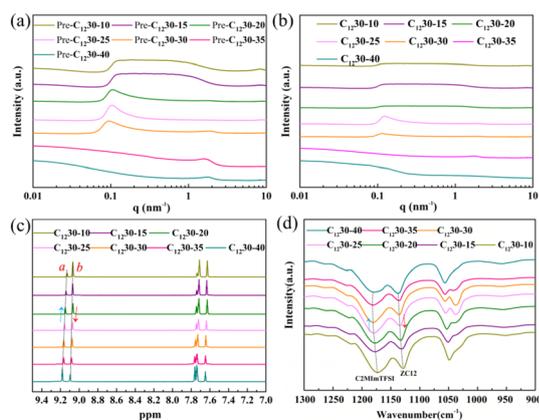

Fig. 3 SAXS data of heterogels (a) before and (b) after UV curing. (c) ^{1}H NMR spectra of the C2 position hydrogen of imidazolium cation in ZC12 (Ha) and C₂MImTFSI (Hb). (d) FT-IR spectra showing the interaction of ZC12 and C₂MImTFSI.

along the curved interfaces, which is facilitated by the strong electrostatic interactions with the zwitterions.

3.2 Dynamic rheological behaviors and anti-swelling properties of heterogels

Rheological properties reveal differences in the microstructure, mechanical performance, and potential applications of materials.[41,42] As shown in Fig. 4, all heterogels exhibit solid-like behavior ($G' > G''$) throughout the frequency sweep. However, $C_{12}30$-10, $C_{12}30$-15, and $C_{12}30$-20 show decreased G' and G'' at high frequencies due to the discrete polymer droplets as a discontinuous frame structure within the continuous medium, which dissipate energy through droplet deformation and rupture.[42] In contrast, for the bicontinuous structured $C_{12}30$-25, the interpenetrating hydrophilic and hydrophobic phases form a 3D network, requiring higher yield stress for structural failure. Thus, $G' > G''$ is throughout the frequency sweep range, as shown in Fig. 4b. As shown in Fig. 4c, higher zwitterion contents induce salting-out, significantly increasing G' and reducing tan δ, which results in excessive rigidity unsuitable for flexible sensors. Thus, the balanced flexibility and strength of $C_{12}30$-25 make it ideal for use in ionic flexible sensors.

The performance of ionic flexible sensors is susceptible to environmental factors, such as temperature, humidity, and water content, which can cause signal instability and hamper their application in complex environments.[43] Particularly, ionogel materials typically exhibit strong hydrophilicity, making them unsuitable for high-humidity environments.[44] Introducing a hydrophobic phase effectively enhances their anti-swelling properties, as a continuous hydrophobic domain forms an efficient water barrier, minimizing interaction with water molecules.[25] Therefore, we first evaluated the hydrophilicity of the heterogels through contact angle measurements. Since the hydrophobic polymer content is identical across all heterogels, the observed contact angle differences arise from the distinct microstructures. As shown in Fig. 5a and b, the droplet-emulsion heterogels ($C_{12}30$-15, $C_{12}30$-20) exhibit an extremely small contact angle, indicating superhydrophilicity. This also confirms that $C_2MImTFSI$ acts as a continuous phase, while the polymer C12-DMA phase disperses as droplets. In contrast, the contact angle of $C_{12}30$-25 increases abruptly. This

is due to its bicontinuous structure with interpenetrating hydrophilic and hydrophobic phases, exposing more hydrophobic domains and significantly enhancing the hydrophobicity of the heterogel.[25] Further increasing the ZC12 content induces salting-out, where amphiphilic ZC12 self-assembles into high-density domains, creating a "dewatering" effect.[45] Therefore, the heterogels ($C_{12}30$-30, $C_{12}30$-35, and $C_{12}30$-40) exhibit relatively large contact angles.

To more intuitively illustrate the interaction between heterogeneous gels and water molecules, we evaluated the swelling properties of the heterogels in an aqueous environment through swelling ratio tests. As shown in Fig. 5c, the $C_{12}30$-25 exhibited the lowest swelling degree (<10%). Compared with the swelling degree of typical ionogel materials (usually as high as 300–500%),[46] the anti-swelling performance of the $C_{12}30$-25 heterogel was significantly improved, and the hydration and humidity sensitivity of the ionic liquid were reduced. Since most sensors are used in daily environments, we exposed the $C_{12}30$-25 heterogel (with the optimal anti-swelling performance in aqueous environments) to an atmospheric environment to investigate the impact of ambient humidity on the heterogeneous gels under daily conditions, and tested the mass change over time. The indoor ambient temperature was 18–22 °C, and the humidity was 40–56%. As shown in Fig. S2a, the $C_{12}30$-25 heterogel exhibited a negligible mass change of approximately 0.2% in the environment. In addition, considering that the sensors are usually attached to human skin, we further evaluated the swelling degree of the $C_{12}30$-25 heterogel in sweat. As shown in Fig. S2b, after the $C_{12}30$-25 heterogel reached swelling equilibrium in sweat, the swelling degree was 7.6%. This further demonstrates that in improving a material's anti-swelling properties, optimized structural design far outperforms the mere introduction of a hydrophobic phase.[47] Therefore, $C_{12}30$-25 is more suitable for constructing ionic flexible sensors.

3.3 Thermal stability and ion conductivity performance of heterogels

Environmental adaptability and interference resistance determine the reliability and practical application scope of ionic flexible sensors.[48] As the core component of a flexible sensor, the structural integrity and stability of heterogels across a wide
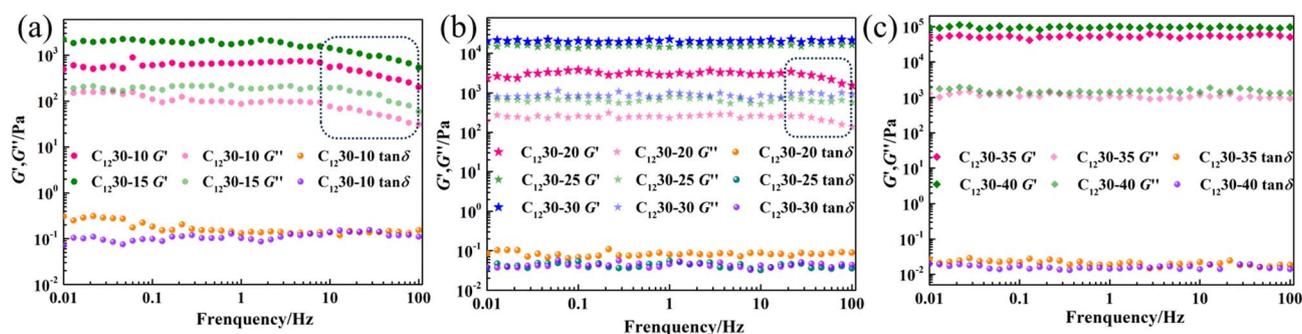

Fig. 4 The rheological property differences of various heterogels ((a) $C_{12}30$-10 and $C_{12}30$-15; (b) $C_{12}30$-20, $C_{12}30$-25 and $C_{12}30$-30; (c) $C_{12}30$-35 and $C_{12}30$-40) under frequency scanning.
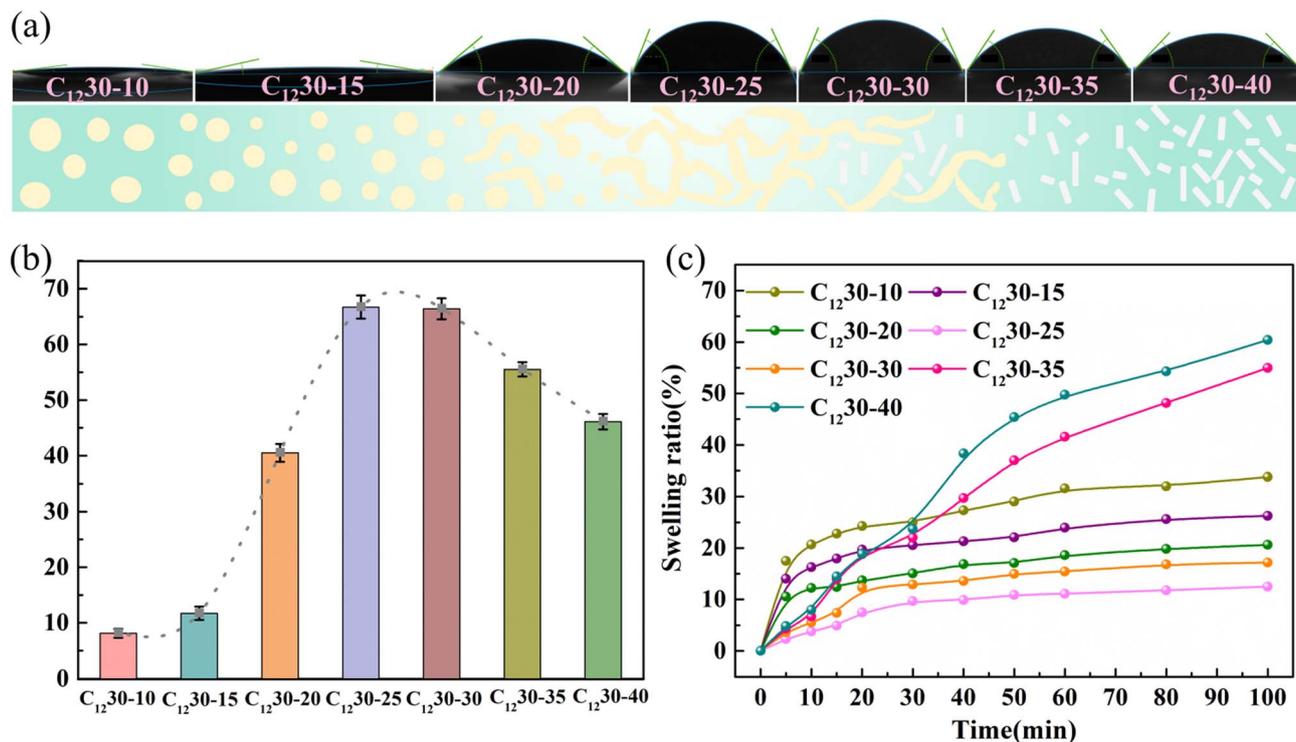
Fig. 5 (a and b) Contact angle of the heterogels and their corresponding microstructure schematics. (c) Swelling ratio of the heterogels.

temperature range are essential for maintaining their sensing functionality. As shown in Fig. 6a, the mass loss of all heterogels is less than 1 wt% at 80 °C/0% RH and almost maintains mass stability, ensuring long-term service life of the core component for ionic flexible sensors. To further investigate thermal stability, TGA tests were conducted (Fig. 6b). The thermal decomposition temperature of heterogels reached 300 °C, preventing sensor failure due to material decomposition at high temperatures. The DTG curve of $C_{12}30$-25 exhibited three decomposition stages corresponding to ionic liquid desorption, framework decomposition, and carbonization of residues. DSC measurements revealed that all heterogels exhibited glass transition temperatures (T_g) below −30 °C (Fig. 6c), maintaining flexibility and elasticity over a wide temperature range. Notably, $C_{12}30$-25 demonstrated a significantly lower T_g. This thermomechanical behavior originates from its bicontinuous architecture, where the continuous, open network with an enhanced interfacial area enables complete permeation of the ionic liquid phase, resulting in maximized plasticization efficiency.[49] Thus, the bicontinuous architecture endows $C_{12}30$-25 with remarkable thermal stability, which constitutes the essential foundation for realizing the sensing performance of the heterogel under diverse temperature conditions.

The heterogel sensor is based on an ion channel sensing mechanism using ions as charge carriers and ionic liquid-rich domains in a bicontinuous structure as ion migration channels. During deformation, the ion conduction rate within the heterogel determines the redistribution and rearrangement of ions in the channels. For ion-conductive flexible sensors, high ionic conductivity is a core advantage. Therefore, we evaluated the ionic

conductivity of heterogels. The ionic conductivity was evaluated using the AC impedance method, and the electrochemical impedance spectroscopy (EIS) of the different heterogels is presented in Fig. S3. As shown in Fig. 6d, $C_{12}30$-25 demonstrated optimal conductivity over the entire temperature range owing to the bicontinuous structure that creates a three-dimensional, low-tortuosity ion transport pathway. Additionally, interfacial zwitterionic groups serve as ion transport sites, significantly enhancing ion transport efficiency. This is critical for improving sensor sensitivity and signal-to-noise ratio. To evaluate the reproducibility of the ionic conductivity performance of the $C_{12}30$-25 heterogel, conductivity cycling measurements ranging from −20 °C to 80 °C were carried out. As shown in Fig. 6e, the ion conductivity–temperature relationship demonstrates excellent reproducibility through 30 cooling–heating cycles, confirming that its ionic transport performance maintains stability even under extreme temperature fluctuations. Furthermore, the temporal stability of the ionic conductivity in the heterogel affects the durability of the sensor. Therefore, $C_{12}30$-25 was exposed to ambient conditions and subjected to a continuous 30-day conductivity test. As shown in Fig. 6f, the ionic conductivity remained relatively stable during 30 days primarily due to the non-volatile nature of the IL and the effective confinement by the biphasic interpenetrating network. The evaluation of the heterogels in terms of thermal stability and ionic conductivity demonstrates that the $C_{12}30$-25 heterogel is suitable for fabricating flexible sensors.

3.4 Sensing performance of heterogels

Owing to the advantages in structure, anti-swelling property, thermal stability and ionic conductivity, $C_{12}30$-25 was employed
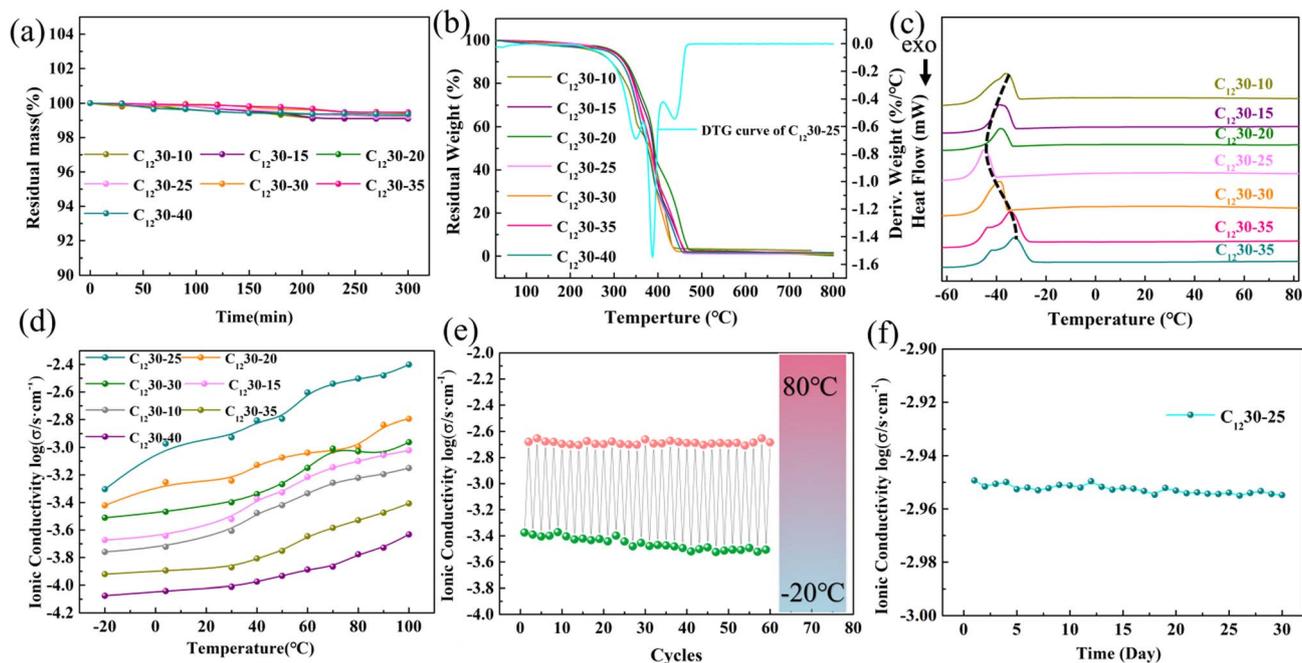
Fig. 6 (a) Plot of the remaining weight *versus* time for different heterogels. (b) TGA test curves of different heterogels and DTG curve of $C_{12}30$-25. (c) DSC measurements of different heterogels. (d) Ionic conductivity changes *versus* temperature curves for the heterogels. (e) Cyclic curve of conductivity of $C_{12}30$-25 at −20 °C and 80 °C. (f) Ionic conductivity changes *versus* time curves for $C_{12}30$-25.

to fabricate the sensor. As shown in Fig. 7a–c, the heterogel sensors attached to the forehead, corners of the mouth or eyes could promptly respond to the deformation caused by facial muscle movements and produce relatively consistent electrical signals during repeated processes. Furthermore, the signal peak shapes exhibit specificity corresponding to different micro-expressions, thus enabling the specific recognition of facial expressions. Typically, the muscle strain induced by eye-blinking is less than 0.1%,[50] with a corresponding average relative resistance change of 3.41%, as depicted in Fig. 7c. The estimated gauge factor (GF) under this strain is as high as 34.1, exhibiting high sensitivity to subtle strains. The average duration of the participants' eye-blinking movement was 0.41 s. The sensor can accurately capture a fast, dynamic signal, demonstrating its favorable response speed. The sensor can also detect minute deformations and vibrations in laryngeal muscles during speech, enabling specific recognition of pronounced words, including "Hi", "Hello" and "Resistance", as shown in Fig. 7d. When repeatedly saying the same word, periodic multi-peak signals can be detected, which can be used to distinguish the pronunciation of different syllables. These multi-peak signals also reflect the sensor's capability to recognize dynamically varying microstrains. Meanwhile, upon repetition of the same word, comparable signals were observed, demonstrating the sensor's high detection accuracy and cycle stability. The monitoring of fine muscle activities provides visual and real-time feedback for auxiliary disease diagnosis and rehabilitation training.

Furthermore, the ionic flexible sensor can perceive different weights, as shown in Fig. 7e, and exhibit excellent reproducibility in detecting minute weights. As the weight increases, the relative resistance change increases. The weight sensitivity of the sensor is shown in Fig. S4. This curve is divided into two regions: in the low-weight region (0–20 g), the weight sensitivity is 1.935% g^{-1}; in the high-weight region (20–200 g), the weight sensitivity is 0.472% g^{-1}. This indicates that the sensor has superior performance in detecting micro-weights. This phenomenon can be ascribed to the predominance of micro–nano structural modulation within the heterogel under low-weight applications, while deformation saturation under high-weight conditions conversely compromises sensing sensitivity.[51]

Thermotactile perception is also a key application of flexible sensors. Affixed to the palm, the sensor generates distinct resistance signals when grasping cups at different temperatures (Fig. 7f). As the temperature increases, the relative resistance variation decreases accordingly. Repeated grasping at the same temperature shows good signal reproducibility and stability. The ability to distinguish water temperatures verifies excellent thermotactile performance, with promising potential for robotic clinical care applications.[51] To evaluate the signal stability and reproducibility of the sensor at different temperatures, the sensor was attached to the lateral joint area of the index finger, and continuous monitoring was conducted during repeated 90° flexion at 0 °C and 45 °C, respectively.

As shown in Fig. S5, the relative resistance change maintained stable output and exhibited excellent reproducibility over 200 consecutive flexion cycles at 0 °C and 45 °C. The robust performance is underpinned by the $C_{12}30$-25 heterogel's inherent ability to maintain structural stability and viscoelasticity over a broad operational temperature window.
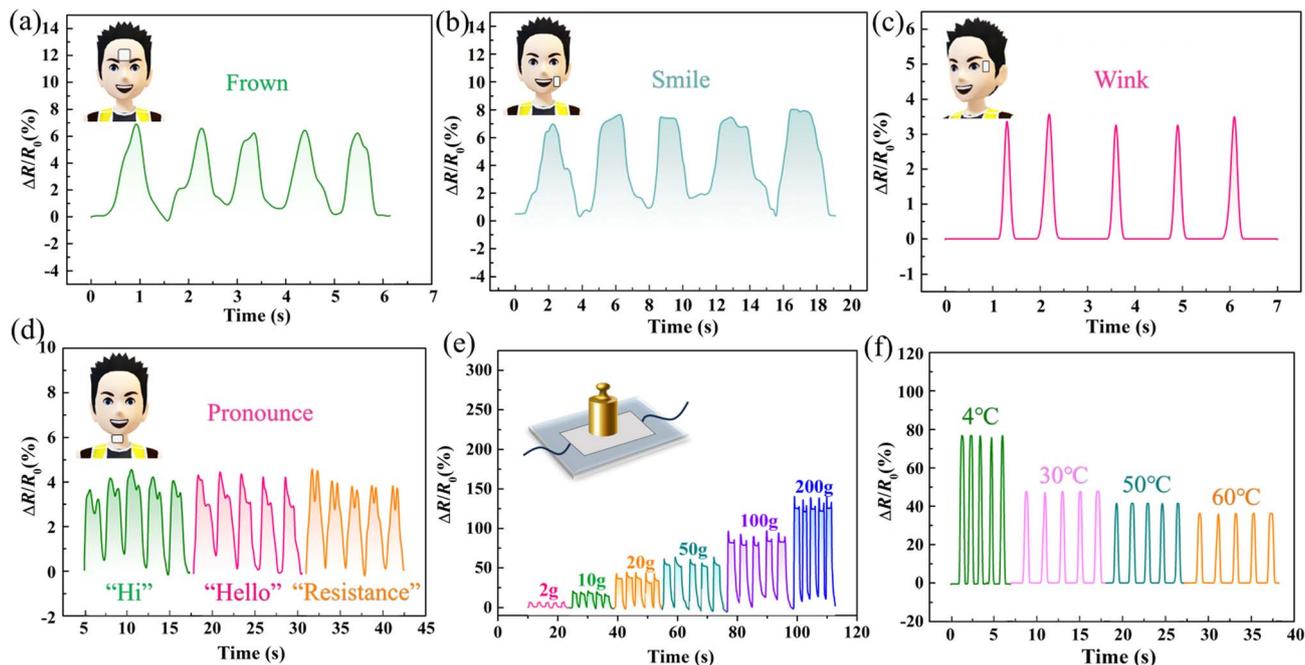
Fig. 7 Sensing and monitoring capability of subtle muscle activities on the face and throat: (a) frowning, (b) smiling, (c) winking and (d) saying the words "Hi", "Hello" and "Resistance". (e) Relative resistance changes *versus* different weights. (f) Relative resistance changes when grasping water cups at different temperatures.

4. Conclusion

In summary, microstructure engineering serves as a critical strategy for developing high-performance ionic flexible sensors. Inspired by the tunable micro/nanostructures of emulsions, a heterogel with bicontinuous ionic channels was constructed using ionic liquid-emulsion templates. Ionic liquids as the polar phase transform these gels from structural materials into high-performance smart platforms, demonstrating significant potential in flexible sensing applications. The introduction of the hydrophobic phase reinforces the gel framework and addresses the humidity sensitivity of ionogel materials, thereby expanding the application scope. Furthermore, the densely packed zwitterionic groups at the interface provide long-range, efficient ion transport sites. Benefiting from high ion transport rates, the resulting sensors accurately detect subtle muscle movements and enable the specific recognition of speech, weight, and temperature. This work provides new insights into the design of intelligent ionic flexible sensors with potential applications in health monitoring and human–machine interaction.

Author contributions

Yufan Wang: writing – original draft, investigation, formal analysis, data curation. Yue Wang: writing – original draft, investigation, formal analysis, data curation. Li Qin: visualization, software, investigation. Zhuo Zhang: visualization, investigation. Yang Yu: writing – review & editing, supervision, investigation, funding acquisition, conceptualization.

Conflicts of interest

The authors declare that they have no known competing financial interests or personal relationships that could have appeared to influence the work reported in this paper.

Data availability

All relevant data are provided within the article and its supplementary information (SI).

Supplementary information: ^{1}H NMR spectrum and proton assignments of ZC12; sample composition; the weight change over time of C_{12}30-25 heterogel at ambient temperature 18–22 °C and the humidity 40–56%; the swelling ratio of C_{12}30-25 heterogel in sweat; the electrochemical impedance spectroscopy (EIS) of different heterogels; the correlation curve between relative resistance change and weight; relative resistance changes. When the finger was subjected to continuous 90° bending for 200 s at 0 °C and 45 °C, respectively. See DOI: https://doi.org/10.1039/d5ra09922f.

Acknowledgements

References

1 Y. Cho, J. W. Baek, M. Sagong, S. Ahn, J. S. Nam and I. D. Kim, *Adv. Mater.*, 2025, **37**, 2500162.

2 H. Cho, Y. R. Kim, J. Kim, S. Lee, S. Jung, J. Kim, J. Kim, Y. J. Park, S. P. Kim and H. Ko, *Mater. Horiz.*, 2025, **12**, 6241–6251.

3 A. Wahaba, L. Ara, M. T. Khana, L. A. Shah and H. Yoo, *Colloids Surf., A*, 2025, **720**, 137202.

4 J. Kim, D. H. Kang, M. S. Kwak, G. Jung, J. Kim, S. Park, H. Ko and V. V. Tsukruk, *ACS Appl. Mater. Interfaces*, 2025, **17**, 59994–60027.

5 Y. Cao, Y. Peng, W. Ren, H. Wang, Y. Diao and Z. Liu, *Sci. Bull.*, 2025, **70**, 2784–2796.

6 Z. Ye, C. Zhang, G. Pang, K. Xu, S. Liu, Y. Wang, J. Qiu, H. Dai, B. Wang, Y. Gan, L. Yang, H. Yang and G. Yang, *Adv. Sci.*, 2025, e16816.

7 R. Yuan, L. Lv, F. Wang, Y. Yu, S. Zhang, J. Yin and R. Huang, *Colloids Surf., A*, 2025, **727**, 138249.

8 K. Sharma, K. Bhunia, S. Chatterjee, M. Perumalsamy, A. A. Saj, T. Bhatti, Y. C. Byun and S. J. Kim, *Nano-Micro Lett.*, 2025, **18**, 63.

9 Y. M. Yuan, B. Liu, M. R. Adibeig, Q. Xue, C. Qin, Q. Y. Sun, Y. Jin, M. Wang and C. H. Yang, *Adv. Mater.*, 2024, **36**, 2310429.

10 M. S. Kim, J. H. Kim, H. Y. Yoo, D. S. Yoon, D. H. Park, C. Y. Lee, S. J. Kim, S. B. Choi, K. Hong and K. H. Lee, *ACS Mater. Lett.*, 2024, **6**, 4658–4666.

11 Y. Tang, Z. Lin, S. Chen and X. Xiao, *Colloids Surf., A*, 2025, **723**, 137344.

12 J. Chen, Y. Gao, L. Shi, W. Yu, Z. Sun, Y. Zhou, S. Liu, H. Mao, D. Zhang, T. Lu, Q. Chen, D. Yu and S. Ding, *Nat. Commun.*, 2022, **13**, 4868.

13 J. Hamonnet, I. E. Nylund, P. Kontis, W. Hua, P. Alonso-Sánchez, J. R. Zuazo, M. V. Blanco and A. M. Svensson, *ACS Appl. Mater. Interfaces*, 2025, **17**, 52112–52124.

14 M. Mirzaei-Saatlo, E. Asghari and H. Shekaari, *J. Energy Storage*, 2025, **108**, 115069.

15 X. Fan, S. Liu, Z. Jia, J. J. Koh, J. C. C. Yeo, C. G. Wang, N. E. Surat'man, X. J. Loh, J. L. Bideau, C. He, Z. Li and T. P. Loh, *Chem. Soc. Rev.*, 2023, **52**, 2497–2527.

16 X. Luo, H. Wu, C. Wang, Q. Jin, C. Luo, G. Ma, W. Guo and Y. Long, *Chem. Eng. J.*, 2024, **483**, 149330.

17 Z. Ren, N. Liu, Q. Zhang, J. Yin, P. Jia, W. Lu, Q. Yao, M. Deng and Y. Gao, *Adv. Sens. Res.*, 2023, **2**, 2200099.

18 X. Chen, X. Xia and C. F. Guo, *Adv. Funct. Mater.*, 2025, e12920.

19 Y. Wang, C. Ge, M. Wang, J. Ma, Y. Zhou, S. Wang, M. Liu, Q. Gao, F. Zhao, Q. Cheng, F. Wen, Y. Liu, H. Shen, L. Li and T. Zhang, *Adv. Funct. Mater.*, 2025, **35**, 2425225.

20 C. Zhao, Y. Wang, G. Tang, J. Ru, Z. Zhu, B. Li, C. Guo, L. Li and D. Zhu, *Adv. Funct. Mater.*, 2022, **32**, 2110417.

21 H. Jin, Z. Zhu, H. Li, N. Kang, M. E. L. Mansori and W. Zhang, *Adv. Colloid Interface Sci.*, 2025, **344**, 103600.

22 X. Yan, J. Zhang, Y. Sheng, K. Chen, H. Zhao, Q. Zhang, Y. Cheng, Z. Ge, X. Ming and Y. Zhang, *ACS Nano*, 2025, **19**, 40579–40593.

23 H. Zhang, Z. Mao, J. Zhang, Z. Zhang, S. Chabi and N. Abidi, *Polym. Rev.*, 2024, **64**, 1098–1135.

24 X. He, B. Zhang, Q. Liu, H. Chen, J. Cheng, B. Jian, H. Yin, H. Li, K. Duan, J. Zhang and Q. Ge, *Nat. Commun.*, 2024, **15**, 6431.

25 L. Han, C. Shan, M. Cui, R. Su and R. Huang, *Small*, 2025, **21**, e06902.

26 H. Ma, M. Wang, J. Hou, X. Wang, P. Sun and F. Wang, *Adv. Mater.*, 2025, **37**, 2500770.

27 L. Xiang, Q. Li, C. Li, Q. Yang, F. Xu and Y. Mai, *Adv. Mater.*, 2022, **35**, 2207684.

28 X. Li and X. Huang, *Colloids Surf., A*, 2022, **655**, 130254.

29 Y. Qian, L. Su, H. Jing, C. Chai, F. Xie, X. Qiu and J. Hao, *Carbon Energy*, 2025, **7**, e697.

30 H. Zhai, W. Qin, Y. Wang, C. Gu, M. Chen, L. Ge, S. Xue, X. Li, X. Zhao, Y. Xu, Z. Ming, S. Li and S. Yin, *Adv. Funct. Mater.*, 2025, **35**, 25051719.

31 U. H. Choi, M. Lee, S. Wang, W. Liu, K. I. Winey, H. W. Gibson and R. H. Colby, *Macromolecules*, 2012, **45**, 3974–3985.

32 X. Gao, F. Lu, L. Shi, H. Jia, H. Gao and L. Zheng, *ACS Appl. Mater. Interfaces*, 2013, **5**, 13312–13317.

33 K. Matuszek, S. L. Piper, A. Brzęczek-Szafran, B. Roy, S. Saher, J. M. Pringle and D. R. MacFarlane, *Adv. Mater.*, 2024, **36**, 2313023.

34 M. Xu, F. Liu, L. Chen, Y. Lei, Z. Liu, T. Abdiryim, F. Xu, J. You, Y. Tan, Z. Tan and X. Liu, *Energy Storage Mater.*, 2025, **80**, 104373.

35 G. Jiang, W. Zou, W. Zhang, Z. Ou, S. Qi, T. Ma, Z. Cui, Z. Liang and L. Du, *Adv. Energy Mater.*, 2024, **14**, 2303672.

36 X. Hao, M. Gao, R. Zhang, Y. Tang, X. Mu, Y. Zhao, Y. Lu and X. Zhou, *Adv. Funct. Mater.*, 2025, **35**, 2416317.

37 M. C. S. Fernandes, R. Branco, P. Pereira, J. F. J. Coelho, P. V. Morais and A. C. Serra, *Biomacromolecules*, 2024, **25**, 7915–7925.

38 K. Cui, Y. N. Ye, T. L. Sun, C. Yu, X. Li, T. Kurokawa and J. P. Gong, *Macromolecules*, 2020, **53**, 5116–5126.

39 S. Li, H. Hong, D. Li, X. Yang, S. Wang, D. Zhang, Q. Xiong, Z. Huang and C. Zhi, *Angew. Chem., Int. Ed.*, 2025, **64**, e202409500.

40 G. Zhang, T. Zhang, Z. Zhang, R. He, Q. Wang, S. S. Chi, Y. Cui, M. D. Gu, Z. Liu, J. Chang, C. Wang, K. Xu and Y. Deng, *Nat. Commun.*, 2025, **16**, 4722.

41 X. Peng, Y. Liu, J. Li, Q. Chi, X. Zhao, X. Tong, H. Wang and L. Jiang, *Food Res. Int.*, 2025, **220**, 117113.

42 J. Mao, X. Zhou, C. Feng, W. Ye, A. Ruzibayev, A. Fayzullaev, M. A. Cerqueira and Z. Meng, *Food Chem.*, 2025, **493**, 145790.

43 K. Choi, G. Lee, M. G. Lee, H. J. Hwang, K. Lee and Y. Lee, *Nano-Micro Lett.*, 2025, **17**, 180.

44 J. Zhang, J. Mei, C. Liu, K. Guan, X. Chen, Y. Wang, X. Liu, W. Pei, Y. Xu, Y. Wang, X. Zhang and G. Qiu, *J. Mater. Chem. A*, 2025, **13**, 22859–22870.

45 H. Yin, M. You, X. Shi, H. Yu and Q. Chen, *Mater. Horiz.*, 2024, **11**, 3946–3960.

46 H. Pan, J. Huang, X. Huang, Y. Liang, N. Shen, L. Kong, L. Fan and R. Jin, *Chem. Eng. J.*, 2025, **520**, 166097.

47 R. Zhou, Y. Jin, W. Zeng, H. Jin, Y. Li, J. Mei and J. Liu, *Adv. Funct. Mater.*, 2024, **34**, 2316687.

48 F. M. Li, Z. Tang, X. H. Chen, H. Q. Li, T. S. Liu, S. F. Li, Y. P. Jiang, X. G. Tang and J. Gao, *Colloids Surf., A*, 2025, **726**, 137938.

49 J. Han, M. J. Lee, K. Lee, Y. J. Lee, S. H. Kwon, J. H. Min, E. Lee, W. Lee, S. W. Lee and B. J. Kim, *Adv. Mater.*, 2022, **35**, 2205149.

50 B. Xu, M. Yang, W. Cheng, X. Li, X. Xu, W. Li, H. Zhangand and M. Zhou, *Nat. Commun.*, 2025, **16**, 7920.

51 L. Ye, Z. Tang, J. Feng, Y. Jiang, X. Tang, Y. Zhou, X. Xing and J. Gao, *Chem. Eng. J.*, 2025, **519**, 164866.